PAPER

Check for updates

Preparation and properties of a UV-curable coating containing rare earth CeO$_2$

Yihua Sun, Guoyao Li and Rong Zhong (ID) *

A UV-curable coating with UV and blue light protection was prepared by incorporating modified rare earth nano cerium dioxide (CeO$_2$) treated with the silane coupling agent KH570. The structures of the modified CeO$_2$ and the resulting UV-curable coating were characterized using Fourier Transform Infrared Spectroscopy, X-ray diffraction, scanning electron microscopy, and thermogravimetric analysis. UV spectral analysis was conducted to evaluate the UV shielding performance of the coating. The results demonstrated that the nano-CeO$_2$ was uniformly distributed within the polymer matrix of the cured coating. The coating exhibited UV shielding capabilities ranging from 58% to 98% in the UVB region (280–315 nm), as well as effective protection against blue light (400–450 nm), and the visible light transmittance is maintained at about 90%. The UV-cured coating also displayed excellent mechanical properties, indicating its potential application in electronic products.
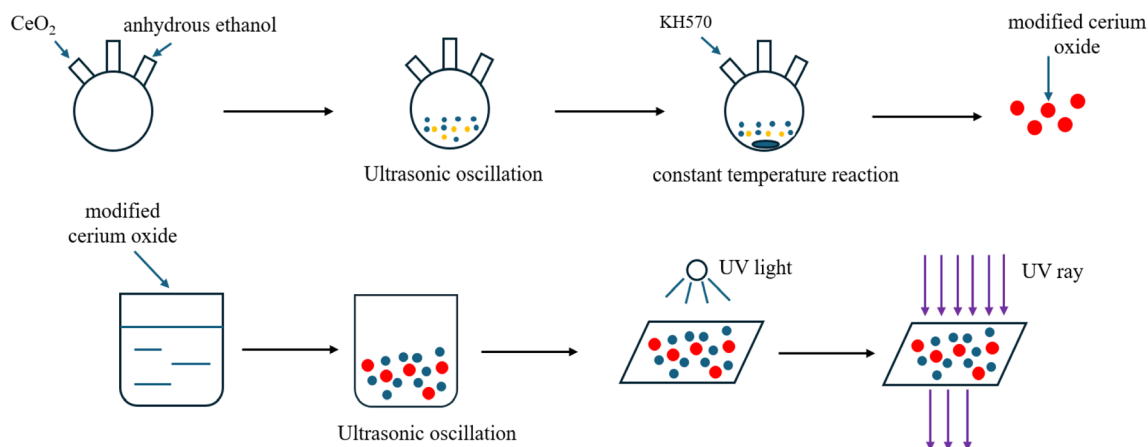
1. Introduction

Light curing technology has gained recognition as a sustainable approach characterized by the "5Es," namely, economy, efficiency, energy conservation, environmental protection,[1–6] and extensive applicability, with widespread utilization in coatings,[7–10] adhesives, 3D printing, and biomedical fields.[11–15] However, the suboptimal mechanical performance of light-cured polymers has critically constrained their industrial implementation. This study posits that the strategic integration of inorganic nanoparticle fillers addresses these limitations by simultaneously enhancing composite durability through improved surface hardness, fracture resistance, and dimensional stability, while maintaining the ecological advantages inherent to photopolymerization processes.[16] Light curing technology is acclaimed as a sustainable approach that has applications across domains that include coatings, adhesives, 3D printing, and medical materials, owing to its unique advantages. Nevertheless, the practical use of light-cured polymer materials has faced limitations due to their subpar physical properties. To mitigate this issue, the incorporation of rigid materials has emerged as a promising solution. Inorganic nanoparticles are frequently employed as filler materials, with additional benefits to composites, such as enhanced surface hardness, improved toughness, and minimized polymerization shrinkage stress. Some modified polymeric materials can obtain new functionality.[17]

Currently, inorganic fillers are doped into light-curing polymers using methods such as blending,[18–20] sol–gel processing,[21,22] intercalation,[23–25] and *in situ* reactions.[26–28] The particle size of the inorganic fillers is typically controlled within the nanometer range, *i.e.*, below 100 nm. This approach allows for a more uniform dispersion of the inorganic phase within the organic matrix, a more structurally ordered composite, and stronger interfacial interactions, all of which contribute to improved overall coating performance.[29] Zhigang Yuan *et al.*[30] investigated the effect of different concentrations of nano cerium oxide on the properties of epoxy resin nanocomposites. The results showed that adding a suitable amount of nano cerium oxide altered the mechanical and thermal stability of the composites. Dayu Liang *et al.*[31] examined the impact of stearic acid-modified cerium oxide nanoparticles (n-CeO$_2$) on epoxy resin nanocomposites and explored the corresponding modification mechanism. Their findings revealed that the carboxyl groups of stearic acid formed ligand bonds or electrostatic interactions with Ce^{3+} or Ce^{4+} ions on the surface of n-CeO$_2$, allowing the modified nanoparticles to disperse more uniformly in the polymer matrix. When the content of modified cerium dioxide (CeO$_2$) nanoparticles reached 2 wt%, the mechanical properties and thermal stability of the composites were significantly enhanced. Xiaochen Yu *et al.*[32] synthesized modified CeO$_2$(mCeO$_2$) by treating CeO$_2$ with 3-(methacryloyloxy)propyltrimethoxysilane (KH570). Subsequently, polyurethane acrylate was modified using mCeO$_2$ to prepare polyurethane acrylate/modified CeO$_2$(PUA/mCeO$_2$) composites with UV-absorbing properties. It was observed that the composites exhibited excellent performance when the content of modified nano cerium oxide reached 2 wt%.

Department of Materials and Chemistry, School of Environmental & Chemical Engineering, Nanchang Hangkong University, Nanchang, 330063, China. E-mail: zhongr@nchu.edu.cn; Fax: +86791 83953373; Tel: +86791 83953373

Scheme 1 Preparation of composite materials.

2. Materials and methods

2.1 Materials

Aliphatic urethane acrylate was purchased from Guangzhou Songda New Material Technology Co.Tripropylene glycol diacrylate, pentaerythritol triacrylate, and ethoxylated trimethylolpropane triacrylate were supplied by Guangzhou Boxing New Material Technology Co. 1-Hydroxycyclohexyl phenylketone was obtained from Tianjin Jiuji New Material Co,3-(methacryloyloxy)propyltrimethoxysilane was purchased from Dongguan Kangjin New Material Co., and anhydrous ethanol and nano CeO_2 were obtained from Aladdin.

2.2 Synthesis and characterization of modified nano cerium oxide

Nano CeO_2(5 g)was added to a three-necked flask, followed by the addition of anhydrous ethanol (30 mL), and dispersed using an ultrasonic machine (PS-40A, Shenzhen Chao Yida Science and Technology Co., Ltd) for 3 h to ensure complete dispersion in the solvent. The suspension was then heated in a constant-temperature water bath (ZNCL-B140*140, Henan Shengbo Instrument and Equipment Co., Ltd) to the designated temperature. KH570 was gradually added under magnetic stirring, and the reaction was maintained at the specified conditions for a set duration. The mixture was allowed to cool to room temperature and was subsequently washed twice with anhydrous ethanol and deionized water using a high-speed centrifuge (SN-LSC-1, Shanghai Shangyi Co., Ltd).The final product was dried at 90 °C for 12 h in an electric blast drying oven (101-

00S, Hangzhou Lichen Instrument Technology Co., Ltd) to obtain modified n-CeO_2.

Deionized water (35–55 mL) was added to a separatory funnel, followed by the one-time addition of modified nano cerium oxide (5 ± 0.01 g) (m). Water was then added until the total volume reached 200 mL. The funnel was shaken back and forth at a frequency of 120 times per minute for 1 min, placed horizontally and shaken again for 1 min, and then left to stand on a funnel stand for 2 h. After delamination, the lower layer of the separated phase was collected and weighed (m_1) after drying at a constant temperature. The activation index was determined as the mass fraction w and expressed as a percentage. It was calculated according to the following formula:[33]

$$w = (m - m_1)/m \times 100$$

Each activation index was measured at least three times and averaged.

Fourier Transform Infrared Spectroscopy (FTIR) was used to determine the chemical structure of the modified nano cerium oxide. Spectra were collected using an FTIR spectrometer (Magna 380, Nicolet, USA) within the wave range of 400–4000 cm^{-1}. Powder samples were analyzed by X-ray diffraction (XRD), recorded over 2θ values ranging from 5° to 80°, using a Cu-Kα-ray diffractometer (D8 Advance, Bruker, Germany) operating at 40 kV and 40 mA. Field emission scanning electron microscopy (Nova SEM 450, FEI, USA) was employed to examine the morphology and potential agglomeration of the modified n-CeO_2.

2.3 Preparation and characterization of UV-curable coatings

The preparation of UV-cured coatings was conducted in two stages. In the first stage, SD7549 (25%), DPHA (20%), PETA (42%), TMPTA (5%), and the photoinitiator Irgacure 184 (8%) were added to a disposable plastic beaker under light-avoiding conditions and dispersed using an ultrasonic machine for 30 min. In the second stage, the modified n-CeO_2 were incorporated into the organic coating system *via* ultrasonic dispersion. Once a uniform mixture was achieved, the coating was

applied to glass slides using a 30-mesh wire rod. The coated slides were pre-baked in an oven at 80 °C for 40 s and subsequently cured using a handheld UV radiation curing device (ST1KW230MM, Dongguan Ergu Optoelectronic Technology Co., Ltd). The modified n-CeO$_2$were added as a percentage of the total mass of the formulation.

FTIR was employed to evaluate the binding degree of the modified nanoparticles within the coatings. XRD was used to determine the crystallinity of the nanoparticles in the cured matrix. Scanning electron microscopy (SEM) was used to observe the dispersion of the modified nanoparticles. Thermogravimetric analysis (TGA) was conducted to assess the thermal stability of the samples using a thermogravimetric analyzer (TG-209, PerkinElmer, USA). Tests were performed under a nitrogen atmosphere over a temperature range of 50–1000 °C, at a heating rate of 10 °C min^{-1}, and a nitrogen flow rate of 100.0 mL min^{-1}. Data were recorded at intervals of 0.5 s. UV spectral analysis was performed to determine the UV

shielding properties of the coatings. The absorbance was measured across the 200–500 nm wavelength range using a UV-vis spectrophotometer (Model UV-2550, Shimadzu, Japan).

3. Results and discussion

3.1 Synthesis conditions of modified nano cerium oxide

3.1.1 Effect of reaction temperature. The activation index as well as the particle size of modified n-CeO$_2$are analyzed by varying the reaction temperature (Fig. 1). Fig. 1(a) shows that the activation index of modified n-CeO$_2$ gradually increases, and the particle size gradually decreases as the reaction temperature increases from 50 °C to 70 °C. The activation index reaches its peak value when the reaction temperature reaches 70 °C. At this point, the particle size of the nanoparticles is the smallest. Under the condition that other reaction parameters remain unchanged, as the reaction temperature increases, the activity of the silane coupling agent KH570 increases, the
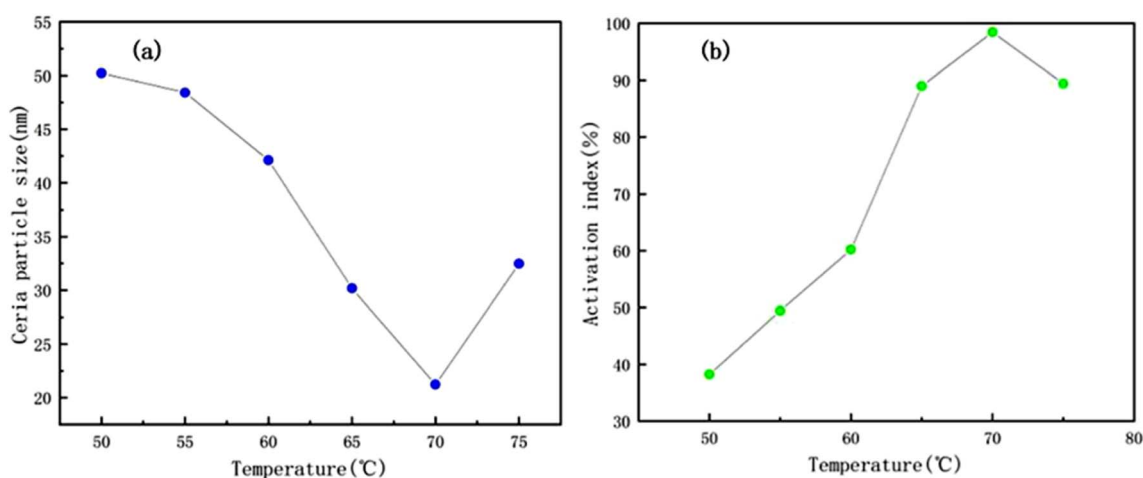

Fig. 1 Particle size analysis of modified CeO$_2$ nanoparticles at different reaction temperatures and activation index plots (a) particle size distribution (b) activation index.
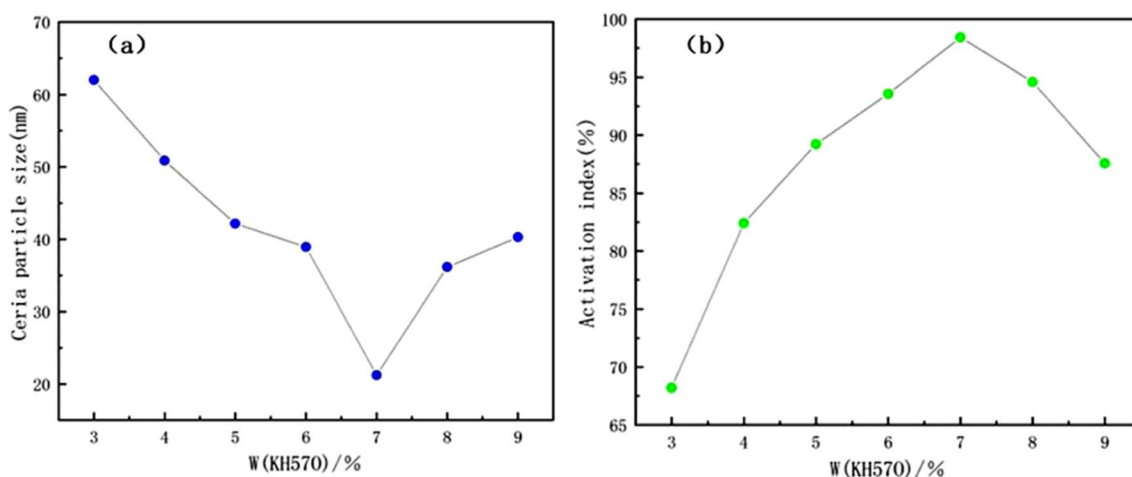

Fig. 2 Particle size analysis of modified CeO$_2$ nanoparticles with different silane coupling agent dosages and activation index plots (a) particle size distribution (b) activation index.
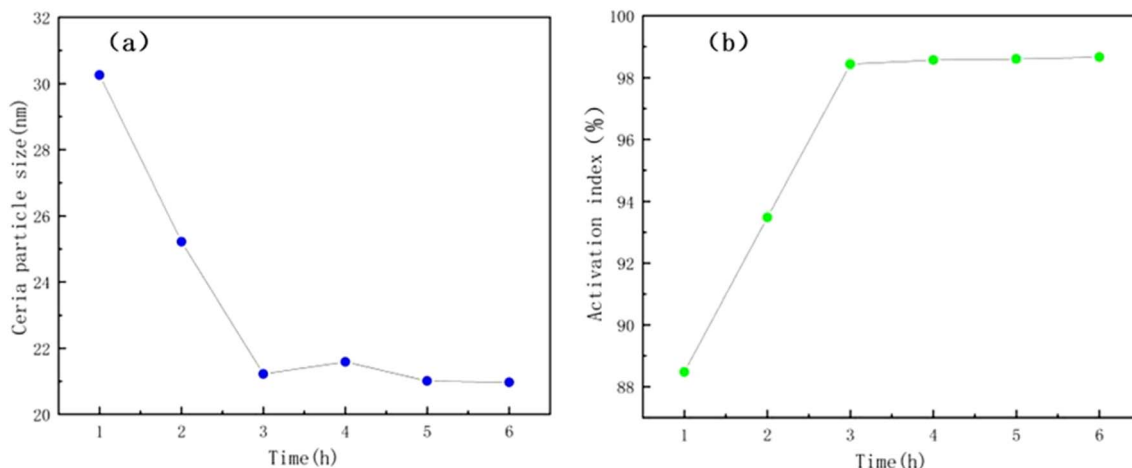
Fig. 3 Particle size analysis of modified CeO$_2$ nanoparticles at different reaction times and activation index plots (a) particle size distribution (b) activation index.

number of activated molecules increases, and more KH570 branches surround the nanometer CeO$_2$ in the system. Due to intermolecular interactions, the cerium oxide disperses more uniformly and is not prone to agglomeration. When the reaction temperature is in the range of 70 °C to 75 °C, the activation index decreases and the particle size gradually increases. When the temperature exceeds 70 °C, KH570 undergoes hydrolysis or crosslinking reactions in the system, which reduces the amount of KH570 encapsulating the CeO$_2$, leading to agglomeration of the n-CeO$_2$.

3.1.2 Effect of silane coupling agent dosage. The activation index and particle size of modified n-CeO$_2$are assessed by varying the amount of silane coupling agent, as shown in Fig. 2. The data indicates that when the dosage of the silane coupling agent (designated as KH570) ranges from 5% to 7%, the activation index of the modified nanoparticles increases alongside the rising dosage of the silane coupling agent. This enhancement is attributed to the increased branching of the silane coupling agent KH570 on the surface of the CeO$_2$ nanoparticles as the dosage escalates. The activation index reaches its maximum at a silane coupling agent dosage of 7%, at which point the modified CeO$_2$ nanoparticles exhibit the smallest particle size. However, when the dosage of the silane coupling agent KH570 is increased beyond 7% and approaches 9%, the activation index begins to decline with rising dosage, and the particle size of the CeO$_2$ nanoparticles increases. This reduction in the activation index is due to the excess silane coupling agent KH570 undergoing cross-linking reactions between molecules, thus resulting in fewer KH570 molecules on the surface of the nanometer-sized CeO$_2$ particles. Consequently, this leads to a greater tendency for the nanoparticles to agglomerate.

3.1.3 Effect of reaction time. The activation index and particle size of modified n-CeO$_2$ were analyzed by varying the reaction time (Fig. 3). As shown, the activation index of the modified CeO$_2$ nanoparticles increases while the nanoparticle size gradually decreases as the reaction time increases from 1 to 3 h. This enhancement in the activity of the silane coupling

agent leads to an increased number of KH570 molecules attached to the surface of the n-CeO$_2$. However, when the reaction time exceeds 3 h, the increase in the activation index of the modified CeO$_2$ nanoparticles becomes insignificant. Beyond 3 h, the surface branching of the silane coupling agent KH570 on the CeO$_2$ nanoparticles reaches a maximum. As a result, even with longer reaction times, there are few unmodified particles remaining. Therefore, the optimal reaction time for this process should be maintained at 3 h.

3.1.4 Factors analysis of experiment results. Through orthogonal experiments, the optimal modification conditions of different consentration coupling agent silane, reaction times, and reaction temperatures were explored. A three factor three-level orthogonal experiment was designed as shown in Table 1. The higher the activation index, the greater the relative molecular weight of the modified nano CeO$_2$ with silane coupling agent KH570. Therefore, this value can indirectly reflect the reaction between silane coupling agent KH570 and nano CeO$_2$ under different reaction conditions.

From Table 2, it can be seen that the range of each factor is $R(C) > R(A) > R(B)$, indicating that the reaction temperature has the greatest impact on the modification results of silane coupling agent KH570, followed by the amount of silane coupling agent added, while the reaction time has the smallest impact on the modification results of silane coupling agent KH570. For the reaction temperature $k_2 > k_1 > k_3$, it indicates that the reaction is easier to proceed when the reaction

Table 1 Three factors and three levels

Levels	Factors		
	A W (KH570)	B h^{-1}	C/°C
1	5	1	65
2	6	2	70
3	7	3	75

Table 2 Data analysis of orthogonal experiment levels

Sample	A	B	C	Activation index/%
1	5	1	70	93.62
2	5	2	75	89.23
3	5	3	65	91.42
4	6	1	75	90.02
5	6	2	65	98.41
6	6	3	70	96.42
7	7	1	65	96.43
8	7	2	70	98.41
9	7	3	75	88.43
$^{a}K_1$	274.27	284.85	283.27	
$^{a}K_2$	280.07	286.05	276.27	
$^{a}K_3$	286.26	288.45	267.68	
$^{b}k_1$	91.42	94.95	94.42	
$^{b}k_2$	93.36	95.35	92.09	
$^{b}k_3$	95.42	96.15	89.23	
^{c}R	4.00	1.2	5.19	

^{a} K is the sum of the factor test results. ^{b} k is the mean value of the sum of the experimental results. ^{c} R is the maximum – minimum of the t values. From the above two tables: $R(C) > R(A) > R(B)$.

temperature is at 70 °C. This may be due to the fact that when the reaction temperature is too low, there are fewer activated molecules in the reaction system, and the reaction does not proceed very thoroughly, resulting in a low activation index. When the reaction temperature is too high, the silane coupling agent KH570 undergoes hydrolysis or crosslinking reactions during the reaction process, resulting in a low activation index of the product. For the dosage of silane coupling agent $k_3 > k_2 > k_1$, it indicates that the optimal dosage of silane coupling agent under this condition is 7%. As the dosage of silane coupling agent gradually increases, the value of activation index also gradually increases, indicating that the surface branching of nano CeO_2 is relatively stable. Compared to the reaction time with the smallest influencing factor, the longer the reaction time, the greater the activation index. It is possible that as the reaction time increases, the number of activated molecules increases, and more nano CeO_2 molecules are attached to the silane coupling agent KH570, resulting in a more thorough reaction. Therefore, the optimal reaction conditions under this orthogonal experiment are: the dosage of silane coupling agent KH570 is 7%, the reaction temperature is 70 °C, and the reaction time is 3 h.
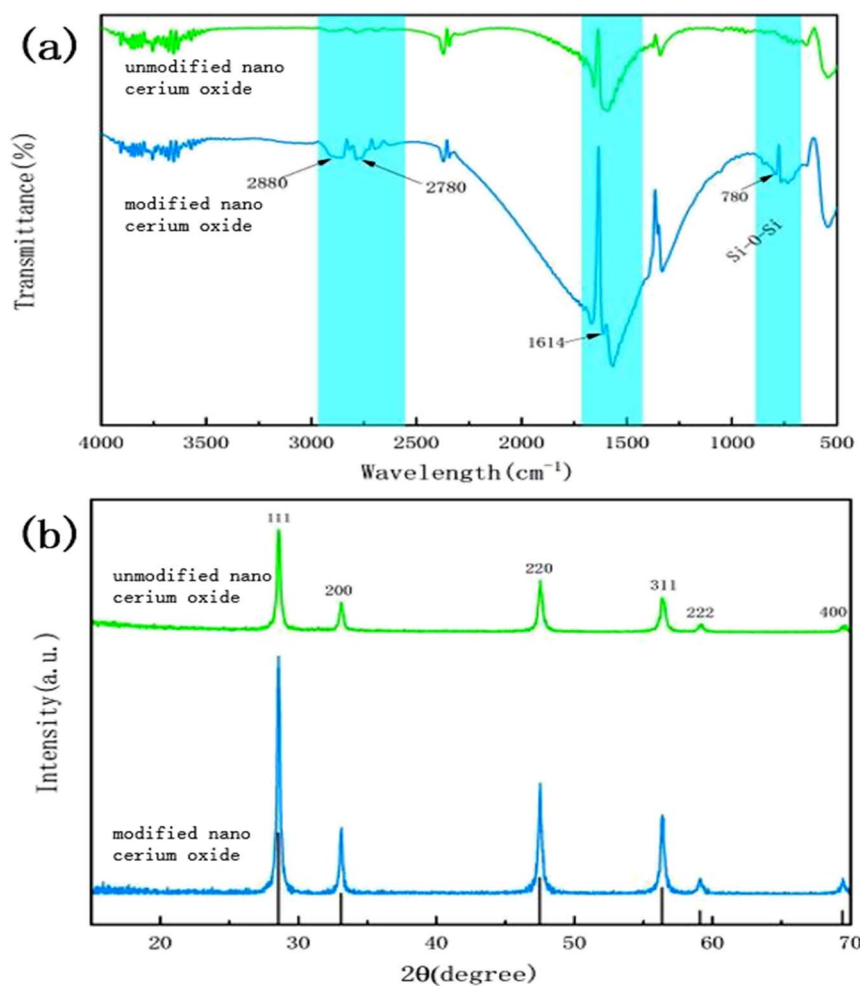

Fig. 4 (a) FTIR spectrum of n-CeO₂ and unmodified n-CeO₂ (b) X-ray pattern of n-CeO₂ and unmodified n-CeO₂.
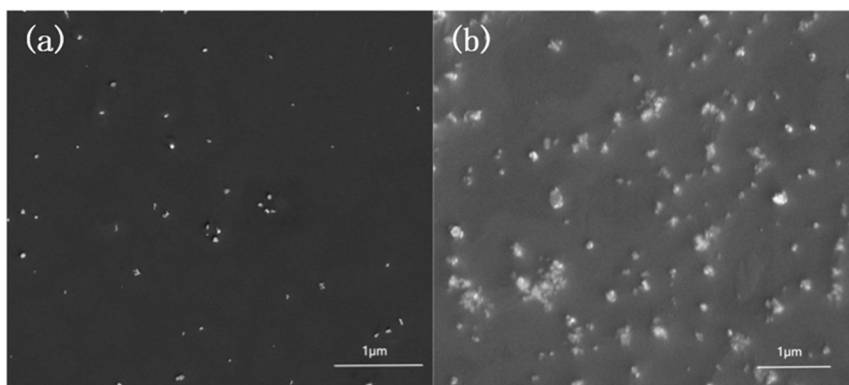
Fig. 5   (a) SEM of modified n-CeO$_2$ (b) SEM of unmodified n-CeO$_2$.

3.2   Characterization of modified n-CeO$_2$

The FTIR spectra of modified n-CeO$_2$ are shown in Fig. 4(a). As illustrated, the newly observed absorption peak at 2880 cm^{-1} corresponds to the characteristic absorption of a methyl group, while the peak at 2780 cm^{-1} is attributed to a methylene group. The absorption band at 1614 cm^{-1} represents the characteristic peak of an alkenyl group. Additionally, the absorption peak at 780 cm^{-1} corresponds to the Si–O–Si bond. These new absorption peaks are consistent with the functional groups present in the silane coupling agent KH570, indicating the successful grafting of KH570 onto the surface of CeO$_2$ nano-powder. Fig. 4(b) presents the XRD pattern of the modified cerium oxide nanopowder. As shown, there is no shift in the position of diffraction peaks between the modified and unmodified CeO$_2$ nanopowders, suggesting that no new crystalline phases were formed during the modification process. However, the intensity of the diffraction peaks of the modified nano-CeO$_2$ powder increases significantly, indicating a higher degree of crystallinity. This enhancement implies smaller grain size and more orderly growth of the crystal planes in the modified nanoparticles.

Fig. 5(a) and (b) show the SEM images of the modified and unmodified n-CeO$_2$, respectively. As observed, the modified CeO$_2$ nanoparticles exhibit more uniform dispersion, smaller particle size, and lack visible agglomeration. The modified CeO$_2$ particles are surrounded by branched organic groups, and their surfaces are encapsulated by these organic chains. As a result, the intermolecular forces are reduced, making agglomeration less likely. In contrast, nano-CeO$_2$ particles inherently possess extremely small particle sizes and, consequently, high surface activation energy. This high activity leads to thermodynamic instability, and the greater the surface activity, the more prone the particles are to agglomeration during storage or handling.

3.3   FTIR spectra of modifiednano-CeO$_2$

The FTIR spectra of the hybridized coatings are presented in Fig. 6. The amino characteristic absorption peak appears at 3400 cm^{-1}, with a notable enhancement in intensity observed in the organic coatings containing modified nano-CeO$_2$ compared to those without the additive. Additional characteristic peaks include: 2815 cm^{-1}: methyl group (–CH$_3$) stretching vibration, 2720 cm^{-1}: methylene group (–CH$_2$–) stretching vibration, and 1614 cm^{-1}: alkenyl (C=C) stretching vibration. A distinct absorption peak at 780 cm^{-1} appears exclusively in the modified CeO$_2$-nanohybridized coating. Becausethe base coating formulation lacks silicon (Si), this peak can be attributed to the Si–O–siasymmetric stretching vibration, confirming the successful grafting of the silane coupling agent (KH570) onto the nano-CeO$_2$ particles.

3.4   XRD of modifiednano-CeO$_2$

Fig. 7 shows the X-ray diffractograms of the modified CeO$_2$ nano-hybridized coating and the unmodified CeO$_2$ nano-hybridized coating. As can be seen, diffraction peaks appear at 2θ = 28.5°, 33.1°, 47.4°, 56.3°, 59.1°, and 69.4° for the modified nano-CeO$_2$ hybridized coated powders, which correspond to the CeO$_2$ standard PDF cards. The diffraction peaks in the figure are clear and sharp, without stray peaks, indicating that the modified CeO$_2$ retains good crystallinity within the hybridized coating. Compared with the unmodified nano-CeO$_2$ at the same additive concentration, the intensity of the modified diffraction peaks does not change significantly.
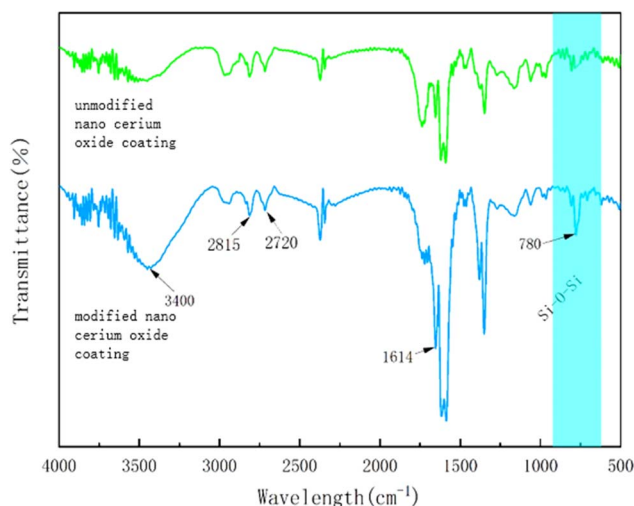

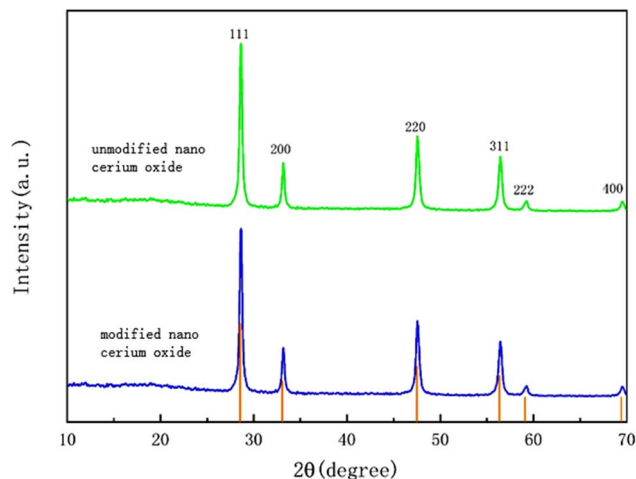Fig. 6   Infrared spectra of hybridized coatings.

Fig. 7   X-ray diffractogram of hybridized coating.

Fig. 9   Thermogravimetric analysis of hybridized coatings.

3.5   SEM of cured coating

The SEM image of the cured coating is displayed in Fig. 8. As can be observed, the modified CeO_2 is more uniformly dispersed within the hybridized coating and shows no signs of agglomeration. The modified CeO_2 nanoparticles are encapsulated by grafted organic structures, which reduces intermolecular attraction and minimizes the likelihood of agglomeration. KH570 is successfully grafted onto the surface of nano-CeO_2, and the modified nanoparticles exhibit smaller particle sizes and more uniform dispersion within the coating. Compared with Fig. 8(a), the modified CeO_2 nanohybrid coating demonstrates a higher degree of dispersion and forms a more ordered structure in the coating matrix.

3.6   TG of UV-cured coating

Fig. 9 shows the TGA of the hybridized coating. As shown, the weight loss of the hybridized coating occurs primarily in two stages. The first stage occurs between 35 °C and 380 °C and is attributed to the volatilization of water molecules in both free and bound states, as well as the evaporation of residual organic solvents present in the hybridized coating. The second stage, occurring between 380 °C and 480 °C, is caused by the thermal
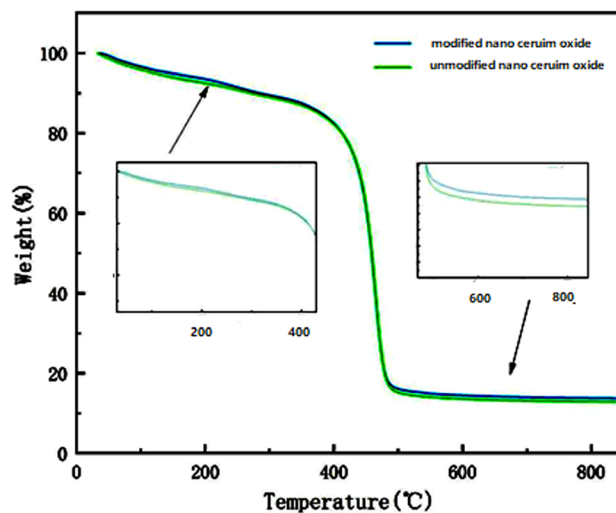
decomposition of organic matter within the hybridized coating. At temperatures beyond 480 °C, the slope of the curve changes only slightly, indicating that the remaining material consists predominantly of inorganic nanoparticles, which are thermally stable and do not decompose. Comparing the two curves in the figure, the thermal stability of the CeO_2 nanohybrid coating modified with the silane coupling agent KH570 is higher than that of the unmodified CeO_2 nanohybrid coating. The modified nano-CeO_2 exhibits higher crystallinity and a more ordered molecular structure. As a result, the polymer chains exhibit reduced molecular mobility and are more resistant to decomposition at elevated temperatures, thereby enhancing the thermal stability of the hybridized coatings.

3.7   UV/blue light absorption of cured coatings containing nano-CeO_2

The UV spectral analysis of the hybridized coatings is shown in Fig. 10. The shielding rate of the hybridized coatings for blue light (400–500 nm) and UVA (200–400 nm) increases with the gradual increase in the additive amount of modified nano-CeO_2. When the modified nano-CeO_2 addition amount was 3%, the
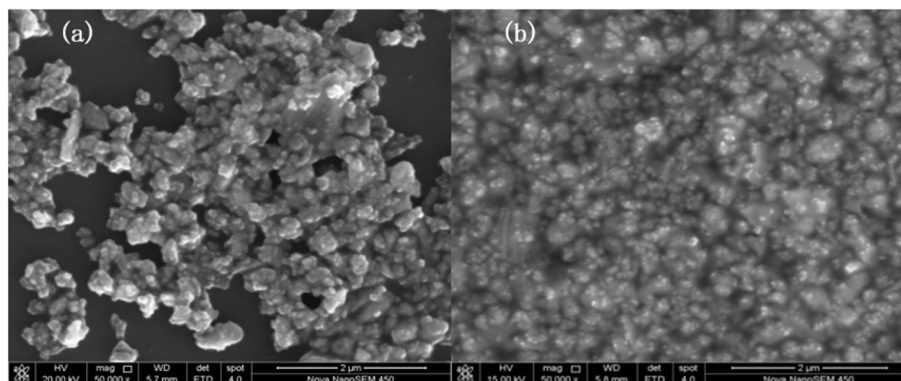

Fig. 8   SEM analysis of the hybridized coating (a) unmodified coating (b) modified coating.
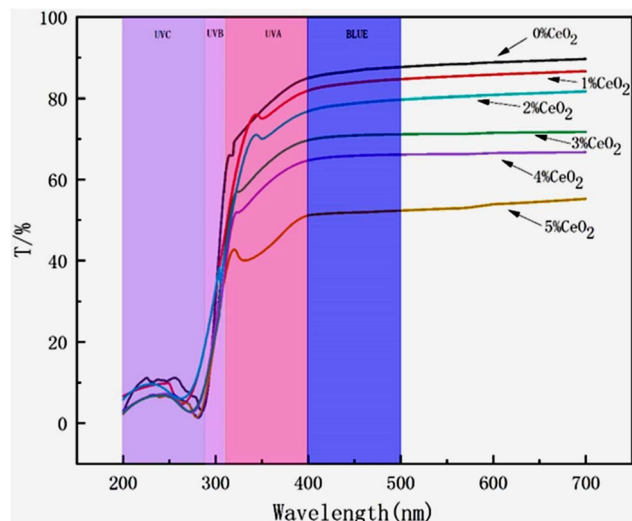
Fig. 10 UV spectral analysis of hybridized coatings.

Table 3 Stability of modified CeO$_2$ nanoparticles in hybridized coatings (— represents no precipitation, + represents a small amount of precipitation, ++ represents a large amount of precipitation)

CeO$_2$/wt%	Standing time/h				
	2	4	12	24	36
4	—	—	—	—	—
4.5	—	—	—	—	—
5	—	—	—	—	+
5.5	+	+	++	++	++
6	+	++	++	++	++

shielding rate of the coating for blue light (400–500 nm) was about 15%, and the shielding rate for UVA (315–400 nm) in the region of 19–35%; the shielding rate for UVB (280–315 nm) in the region of 35–86%. When the modified nano-CeO$_2$ is added in an amount of 4%, the shielding rate of the coating to blue light (400–500 nm) is about 29%, and the shielding rate to UVA (315–400 nm) in the region of 30–45%; the shielding rate to UVB (280–315 nm) in the region of 45–90%. When the modified nano-CeO$_2$ is added in an amount of 5%, the shielding rate of the coating to blue light (400–500 nm) is about 48%, the shielding rate for UVA (315–400 nm) region is 49–60%; the shielding rate for UVB (280–315 nm) region is 58–98%.

3.8 Properties of UV-cured coatings

3.8.1 Stability testing. The stability of different modified n-CeO$_2$ in hybridized coatings is shown in Table 3. As can be seen, when modified CeO$_2$ nanoparticles are added to hybridized coatings at concentrations exceeding 5%, a large amount of precipitation occurs after 12 h of resting. When the modified n-CeO$_2$ are added at 5%, the hybridized coatings exhibit a small amount of precipitation after 36 h of standing. Therefore, in the subsequent study, the addition of modified nano-CeO$_2$ is controlled within the range of 0–5% for preparing the hybridized coatings and investigating their properties.

3.8.2 Mechanical property tests. As illustrated in Table 4, the hardness of the coating exhibited a gradual increase with the incorporation of modified nano-CeO$_2$. Compared with organic coatings, metallic particles inherently possess greater hardness, and their inclusion contributed to enhanced surface hardness of the coating. However, coating flexibility decreased at additive concentrations of 1–5%. Beyond this range, the increased surface rigidity of the coating diaphragm further reduced flexibility. Adhesion performance was also affected by the concentration of nano-CeO$_2$. At 3–5% additive levels, the adhesion grade increased, indicating stronger bonding between the coating and the substrate. This improvement can be attributed to the effect of the silane coupling agent, which enhanced interfacial adhesion. Abrasion resistance was evaluated under a 1 kg load over 2000 rubbing cycles. The results demonstrated that abrasion resistance improved proportionally with increasing nano-CeO$_2$ content. Regarding curing behavior, coatings containing 0–2% modified nano-CeO$_2$ exhibited consistent curing times of 7 s, suggesting minimal influence within this range. However, at higher concentrations (3–5%), curing time increased. This delay may be attributed to reduced light transmission in the film, which impeded deep curing.

4. Conclusions

In conclusion, the optimum modification conditions were investigated in this paper. The results showed that the optimum reaction conditions were 7% dosage of silane coupling agent KH570, 70 °C reaction temperature, and 3 h.

The modified n-CeO$_2$ were mixed with light-curing coatings using the ultrasonic blending method. It was found that the thermal stability of the hybridized coating gradually increased with the increase of the addition of nano-CeO$_2$; in the UV spectral analysis, the shielding rate of the coating against blue light (400–500 nm) was about 48% when the modified nano-CeO$_2$ was added at a rate of 5%, and the shielding rate was 49–

Table 4 Effect of modified nano-CeO$_2$ addition on coating properties (+ represents a small number of scratches, − represents no scratches)

CeO$_2$/wt%	Hardness	Pliability/T	Adhesion	Abrasion performance	Curing time/s
0	2H	9	4B	+	7
1	1H	8	4B	+	7
2	3H	8	4B	—	7
3	4H	6	5B	—	8
4	4H	5	5B	—	9
5	4H	5	5B	—	9

60% in the region of UVA (315–400 nm); the shielding rate of the coating was about 20% in the region of UVB (280–315 nm); the shielding rate in the region of UVA (315–400 nm) is 49–60%; the shielding rate in the region of UVB (280–315 nm) is 58–98%. The UV-cured coating indicated its potential application in electronic products. Compared with past studies, we investigated shielding effects in different wave band electrimanificamt.[34] In current research, there are some shortcomings, such as, insufficient absorption range of electromagnetic waves, insufficient absorption intensity of blue light, and excessive absorption of visible light. These issues are the ones we need to solve in the future.

Data availability

All relevant data are within the paper.

Conflicts of interest

There are on conflicts to declare.

References

1 X. Li, Z. Liu, P. Hong, et al., Synthesis of organic and inorganic hybrid nanoparticles as multifunctional photoinitiator and its application in UV-curable epoxy acrylate-based coating systems, Prog. Org. Coat., 2020, 141, 105565.

2 J. Li, S. Li, Y. Li, et al., In situ monitoring of photopolymerization by photoinitiator with luminescence characteristics, J. Photochem. Photobiol. Chem., 2020, 389, 112225.

3 T. N. Eren, B. Graff, J. Lalevee, et al., Thioxanthone-functionalized 1, 6-heptadiene as monomeric photoinitiator, Prog. Org. Coat., 2019, 128, 148–156.

4 W. Chen, X. Liu, L. Wang, et al., Synthesis and preliminary photopolymerization evaluation of photopolymerizable type II photoinitiators BRA and TXRA, Prog. Org. Coat., 2019, 133, 191–197.

5 Z. Wang, K. Wang, H. Huang, et al., Bioinspired wear-resistant and ultradurable functional gradient coatings, Small, 2018, 14(41), 1802717.

6 Y. Kugimoto, A. Wakabayashi, T. Dobashi, et al., Preparation and characterization of composite coatings containing a quaternary ammonium salt as an anti-static agent, Prog. Org. Coat., 2016, 92, 80–84.

7 M. Salehi, R. Eslami-Farsani, F. Najafi, et al., Preparation and characterization of UV-curable composite containing nano silica for glass-to-glass bonding, Prog. Org. Coat., 2024, 196, 108751.

8 L. Yue, S. Macrae Montgomery, X. Sun, et al., Single-vat single cure grayscale digital light processing 3D printing of materials with large property difference and high stretchability, Nat. Commun., 2023, 14(1), 1251.

9 M. Regehly, Y. Garmshausen, M. Reuter, et al., Holography for linear volumetric 3D printing, Nature, 2020, 588(7839), 620–624.

10 A. M. Herrera-González, J. A. González-López, C. E. Cuevas-Suárez, et al., Formulation and evaluation of dental composite resins with allyl carbonate monomer as eluent for Bis-GMA, Polym. Compos., 2018, 39, E342–E350.

11 M. Pirmoradian, T. Hooshmand, S. Jafari-Semnani, et al., Degree of conversion and microhardness of bulk-fill dental composites polymerized by LED and QTH light curing units, J. Oral Biosci., 2020, 62(1), 107–113.

12 J. Yao, K. Wang and Z. Wang, Effect of hybrid reinforcements on the curing kinetics and mechanical properties of light-cured polymer composites, Polym. Compos., 2024, 45(10), 9588–9599.

13 D. Pieniak, A. Walczak, M. Walczak, et al., Hardness and wear resistance of dental biomedical nanomaterials in a humid environment with non-stationary temperatures, Materials, 2020, 13(5), 1255.

14 B. Pratap, R. K. Gupta, L. Denis, et al., Evaluation of polymerization shrinkage and Vickers hardness for restorative dental composites, Mater. Today: Proc., 2020, 21, 1563–1565.

15 H. Chadda, B. K. Satapathy, A. Patnaik, et al., Mechanistic interpretations of fracture toughness and correlations to wear behavior of hydroxyapatite and silica/hydroxyapatite filled bis-GMA/TEGDMA micro/hybrid dental restorative composites, Composites, Part B, 2017, 130, 132–146.

16 W. Fu, L. Wang and J. He, Evaluation of mechanical properties and shrinkage stress of thiol-ene-methacrylate dental composites with synthesized fluorinated allyl ether, J. Mech. Behav. Biomed. Mater., 2019, 95, 53–59.

17 L. Wei, G. Liu, J. Liu, N. Lv, W. Jiang, C. Dong and S. Shang, Conductive Structural Colored Cotton Fabrics with Nonangle-Dependent Colors and Dynamic Thermal Management, ACS Appl. Mater. Interfaces, 2025, 17(14), 21985–21995.

18 T. LChen, R. Zhong and Z. J. Wang, Preparation, Characterization, and Properties of UV-Curable Coating Doped with Nano-SiO$_2$, Materials, 2023, 16(24), 7576.

19 Z. Yang, B. Liu, Y. Chen, et al., Preparation and performance studies of modified graphene oxide/polyaniline composite anticorrosive coatings, Prog. Org. Coat., 2024, 197, 108855.

20 M. Sharif and S. Tavakoli, Chitosan-modified graphene oxide filled photo-curable nanocomposite coating with advanced properties, Polym. Bull., 2024, 1–18.

21 M. Zheng, W. Wen and S. Liu, g-C$_3$N$_4$/TiO$_2$ for gas-phase formaldehyde photodegradation under visible light in the humidity control coatings, J. Taiwan Inst. Chem. Eng., 2024, 154, 105129.

22 M. Çınar and S. Karataş, Synthesis of polyurethane acrylate hybrids containing fluorine and siloxane by the sol-gel method for UV-curable coatings, Polym. Bull., 2023, 80(11), 11975–12001.

23 M. AAhmed, M. A. Shohide, A. M. El-Saeed, et al., Coating effect of polyurethane-layered double hydroxide nanocomposite on steel, Discov. Mater., 2024, 4(1), 42.

24 J. JJu, Y. Wang, M. H. Yu, et al., Anti-corrosion improvement of epoxy coating by the synergistic effect of barrier shielding

and slow-release based on phytic acid intercalated hydrotalcite, *J. Appl. Polym. Sci.*, 2023, **140**(39), e54459.

25 Y. Chen, W. Bai, J. Chen, *et al.*, In-situ intercalation of montmorillonite/urushiol titanium polymer nanocomposite for anti-corrosion and anti-aging of epoxy coatings, *Prog. Org. Coat.*, 2022, **165**, 106738.

26 L. Sun, N. Wang, Y. Wang, *et al.*, Fabrication of an anti-fouling coating based on epoxy resin with a double antibacterial effect *via* an in situ polymerization strategy, *Prog. Org. Coat.*, 2023, **184**, 107837.

27 Z. Liu, X. Pang, K. Wang, *et al.*, Superhydrophobic coatings prepared by the *in situ* growth of silicone nanofilaments on alkali-activated geopolymers surface, *ACS Appl. Mater. Interfaces*, 2019, **11**(25), 22809–22816.

28 X. Chen, Z. Qu, M. Xie, *et al.*, In-situ crosslinking reaction of graphene oxide & waterborne epoxy resin to construct continuous phase anticorrosive coating, *Arabian J. Chem.*, 2024, **17**(6), 105795.

29 F. Liu, A. Liu, W. Tao, *et al.*, Preparation of UV curable organic/inorganic hybrid coatings-a review, *Prog. Org. Coat.*, 2020, **145**, 105685.

30 Z. Yuan, M. A. Hassan, Z. Wang, *et al.*, Curing behavior, mechanical and thermal properties of epoxy-CeO$_2$ nanocomposites, *J. Appl. Polym. Sci.*, 2022, **139**(4), 51529.

31 D. Liang, J. Yang, X. Li, *et al.*, Preparation and physical properties of CeO$_2$ doped and modified epoxy resin composites, *Polym. Compos.*, 2024, **45**(7), 5968–5979.

32 X. Yu, J. Zheng, Z. Zhou, *et al.*, Study on polyurethane-acrylate/cerium dioxide modified by 3-(Methylacryloxyl) propyltrimethoxy silane and its UV absorption property, *J. Appl. Polym. Sci.*, 2021, **138**(31), 50760.

33 M. Liu, Theoretical and Experimental Research on Powder Activation Index, *China Powder Sci. Technol.*, 2015, **21**(3), 80–85.

34 Z. Wang, R. Zhong and T. L. T. Chen, Preparation of UV-Curable Nano-WO3Coating and Its Infrared Shielding Properties, *Nanomaterials*, 2022, **12**, 3920, DOI: **10.3390/nano12213920**.